nature communications

Article

https://doi.org/10.1038/s41467-024-51137-8

A fabrication strategy for millimeter-scale, self-sensing soft-rigid hybrid robots

Received: 22 November 2023

Accepted: 31 July 2024

Hun Chan Lee[1], Nash Elder[1], Matthew Leal[2], Sarah Stantial[1], Elenis Vergara Martinez[3], Sneha Jos[4], Hyunje Cho[1] & Sheila Russo[1] ✉

Soft robots typically involve manual assembly of core hardware components like actuators, sensors, and controllers. This increases fabrication time and reduces consistency, especially in small-scale soft robots. We present a scalable monolithic fabrication method for millimeter-scale soft-rigid hybrid robots, simplifying the integration of core hardware components. Actuation is provided by soft-foldable polytetrafluoroethylene film-based actuators powered by ionic fluid injection. The desired motion is encoded by integrating a mechanical controller, comprised of rigid-flexible materials. The robot's motion can be self-sensed using an ionic resistive sensor by detecting electrical resistance changes across its body. Our approach is demonstrated by fabricating three distinct soft-rigid hybrid robotic modules, each with unique degrees of freedom: translational, bending, and roto-translational motions. These modules connect to form a soft-rigid hybrid continuum robot with real-time shape-sensing capabilities. We showcase the robot's capabilities by performing object pick-and-place, needle steering and tissue puncturing, and optical fiber steering tasks.

Soft robots offer distinct advantages compared to their rigid counterparts. Their compliance, flexibility, and robustness enable a wide range of tasks, including in-pipe inspection[1,2], drug delivery[3,4], search and rescue[5], and minimally invasive surgery[6–9]. To meet the requirements of these applications, researchers have developed soft robots with various actuation, sensing, and control strategies[10,11]. While soft robotics is a rapidly growing field, embedding core soft robot hardware components – actuation, sensing, and control – remains challenging, as it generally involves a manual and time-consuming fabrication process[12,13]. Particularly, as the scale of the robot miniaturizes, this integration process becomes more intricate, thus further increasing fabrication time and reducing repeatability[14,15].

Various actuator technologies have been integrated into soft robots to induce motion, including cable-driven[16,17], pressure-driven[18,19], electrically-responsive[20–23], magnetically responsive[8,9,24], and thermally responsive[25,26] actuators.

Among these actuation strategies, pressure-driven actuators, specifically pneumatic and hydraulic-based actuators, are widely used in soft robotics. These actuators offer advantages such as safety, lightweight, high output force, and large stroke[10]. The fabrication process for pressure-driven soft robots generally involves manufacturing techniques like molding, 3D printing, and film lamination, where inflatable chambers are embedded during the fabrication process[27,28]. Yet, these techniques have been mostly limited to embedding only the actuation system. As a result, these robots typically operate under open-loop control or off-board pressure-driven feedback control. However, pressure-driven feedback control requires intricate control algorithms due to the inherent non-linear, hysteretic behavior of soft robots[11]. Thus, on-board sensor integration is necessary to effectively control these soft robots and pave the way toward autonomy.

Diverse sensing technologies have been integrated into soft robots to enable proprioceptive and exteroceptive sensing (i.e.,

---

[1]Department of Mechanical Engineering, Boston University, Boston, MA, USA. [2]Department of Biomedical Engineering, Boston University, Boston, MA, USA. [3]Department of Biomedical Engineering, Florida International University, Miami, FL, USA. [4]Department of Physics, Boston University, Boston, MA, USA.
✉e-mail: russos@bu.edu

optic[7,29,30], resistive[31–34], capacitive[20,35], and inductive[36,37]) with the goal to enable closed-loop control in future soft robotics applications. These sensors possess bendable and stretchable properties that do not impede the motion of soft robots[38]. Nevertheless, compact and consistent sensor integration into soft robots is hampered due to discrete, manual assembly processes, particularly in the case of millimeter and smaller-scale systems[14,15,39]. As a result, there is a need for manufacturing techniques that enable repeatable and reliable sensor integration within soft robots[39,40]. One effective strategy for addressing this challenge is to employ monolithic fabrication, where both actuators and sensors are created as an integrated unit. This approach serves to reduce manufacturing defects and, simultaneously, enables self-sensing functionality, resulting in a more compact form factor for soft robots[21,23,26,41,42].

Due to their flexible and deformable nature, soft robots exhibit nonlinear, hysteretic, and viscoelastic behavior, making them inherently more difficult to model and control than rigid systems[43]. To address these challenges, both model-based control and model-free control concepts have been introduced[11,28]. The first approach exploits models like constant curvature modeling[44], Cosserat rod theory[45], Bernoulli-Euler beam theory[46], or finite element modeling to control soft robots[47]. Whereas the latter is a data-driven approach, which predicts and controls the robot using machine learning techniques[48,49]. Although both approaches have been showing promising results, these control strategies have several limitations, such as problem oversimplification, computational cost, and the necessity of ample data[11].

Turning a software problem into a hardware problem, challenges in capturing non-linear deformation and motion in soft robots can be addressed by offloading the burden of modeling and control to "physical intelligence"[40,50]. Methods to provide physical intelligence to soft robots are through material selection and mechanical structural design[40,51,52]. By combining rigid, flexible, and soft materials, both the inherent structural compliance of a soft robot and the motion controllability of a rigid robot can be maintained[53–55]. As a result, the concept of a soft-rigid hybrid robot enhances the predictability of a soft robot's motion by following the rigid robot kinematics and the delivery of force toward the desired direction, while concurrently preserving its ability to adapt to its surroundings through its inherent conformability[35,40,50,56].

Thus far, hybrid robots generally required manual fabrication steps to combine soft components (i.e., thermoplastic films) and rigid structures (i.e., cardboard, plastic) using glue or double-sided tape after rigid mechanisms and soft actuators were manufactured separately[53,57,58]. While these bonding methods are suitable for centimeter-scale and larger robots, they pose challenges in fabricating millimeter-scale and smaller robots[39]. These methods can result in a long fabrication time, difficulties in batch fabrication, and inconsistent manufacturing outcomes as the size of the robot scales down[10,40]. A solution proposed to address this combined the pop-up book MEMS fabrication approach[59,60] with techniques borrowed from soft lithography and silane coupling agents to bond rigid components and PDMS-based soft actuators demonstrating millimeter-scale "soft pop-up" robots[35]. However, this fabrication technique is sensitive to ambient conditions (i.e., temperature and humidity)[61] and is time-dependent (i.e., the time window of the surface activation by oxygen plasma treatment is limited)[62]. These sensitivities and dependencies on environmental and procedural factors can introduce challenges in the fabrication process, necessitating careful control and management of these variables to ensure successful production.

In this work, we present a manufacturing paradigm for millimeter-scale soft-rigid hybrid (SHY) robots (Fig. 1a) that enables monolithic integration of actuator, mechanical controller, and sensor components, with minimal manual assembly required and a compact form factor (Fig. 1b). We employ heat-sensitive acrylic adhesive films to bond the robots' constituent materials. The use of this adhesive film has been explored in previous studies for bonding various rigid and flexible materials, such as metals, plastics, and composites[59,60]. However, this method was not applicable to soft materials or the construction of thermoplastic-film-based soft actuators because the bonding temperature of acrylic adhesive films (i.e., >182 °C) exceeds the melting point (i.e., 120 °C[63]) of thermoplastic films. Here, we introduce the use of polytetrafluoroethylene (PTFE) films, which have a high melting temperature (i.e., 327 °C) to create soft-foldable inflatable actuators (Fig. 1c). We perform permanent chemical surface modification of the PTFE films with hydrogen gas (H_2) plasma to promote adhesion and permanent bonding through lamination via heat and pressure. The final desired motion of the resulting robots is mechanically encoded by rigid-flexible mechanisms, resulting in consistent and controlled motion output. An ionic fluid drives the motion of the proposed robots and also serves as a sensing medium. By embedding an electrical circuit onboard (electrodes) (Fig. 1d) within its constituent materials, the robot can self-sense the change in its encoded motion by measuring the change in resistance across its body. We demonstrated this approach by creating three distinct SHY robotic modules, each capable of self-sensing its unique degrees of freedom, namely translational, bending, and roto-translational movements (Fig. 1e). We showcased the scalability of our fabrication method by manufacturing the SHY robotic modules in different scales (i.e., 5 and 11.5 mm in outer diameter). We performed extensive mechanical characterizations of each robotic module, including range of motion, force and torque, power density, and fatigue testing. To showcase the potential use of the proposed robotic technology, we built a self-sensing soft-rigid hybrid continuum robot (Fig. 1f). With this robot, we demonstrated real-time shape-sensing using embedded ionic resistive sensors. Finally, we integrated various end effectors, including a robotic grasper (manufactured using the same approach), a needle, and an optical fiber onto the SHY continuum robot and performed robotic pick-and-place of soft and hard objects with various shapes and sizes, needle steering and tissue puncturing, and optical fiber steering tasks.

Results

SHY Robot design

Our SHY Robots are designed to start in a flat, two-dimensional configuration, when not pressurized, and can be unfolded into complex 3-D shapes by inflating an embedded soft-foldable actuator (Fig. 1e). The soft-foldable actuator consists of a series of pouch-like balloons made of PTFE films (Fig. 1c). Similar to other thermoplastic film-based soft actuators[6,50,53,57,63], the proposed PTFE-based actuators are soft and flexible (Supplementary Movie 1). This allows the actuators to expand like balloons and conform according to external forces, producing simple linear motion upon pressurization. However, unlike other thermoplastic films, PTFE can withstand higher temperatures, making it a more suitable choice for layer-by-layer lamination-based manufacturing processes that utilize heat-sensitive adhesive films (Fig. 1b). Using this technique, soft-foldable actuators can be seamlessly laminated with other film materials possessing diverse mechanical and electrical properties (i.e., rigid, flexible, soft, and conductive) with minimal manual assembly steps. This monolithic integration enables the incorporation of mechanical structures and conductive layers, facilitating the integration of actuation, sensing, and mechanical controllers into small-scale soft robots. In this paper, we fabricated SHY robotic modules in two different sizes, 5 mm (Supplementary Fig. 2) and 11.5 mm in outer diameter (OD) to demonstrate the scalability of our approach. These modules lie in a flat state at around 1.1 mm and 1.7 mm and possess minimum feature sizes in the micrometer scale.

The PTFE-based soft-foldable actuator consists of a stack of thin PTFE films (i.e., 25 µm in thickness). This soft-foldable actuator functions as a fluid chamber, which holds fluid and causes the actuator to expand upon inflation. Much like the inflation of an inextensible

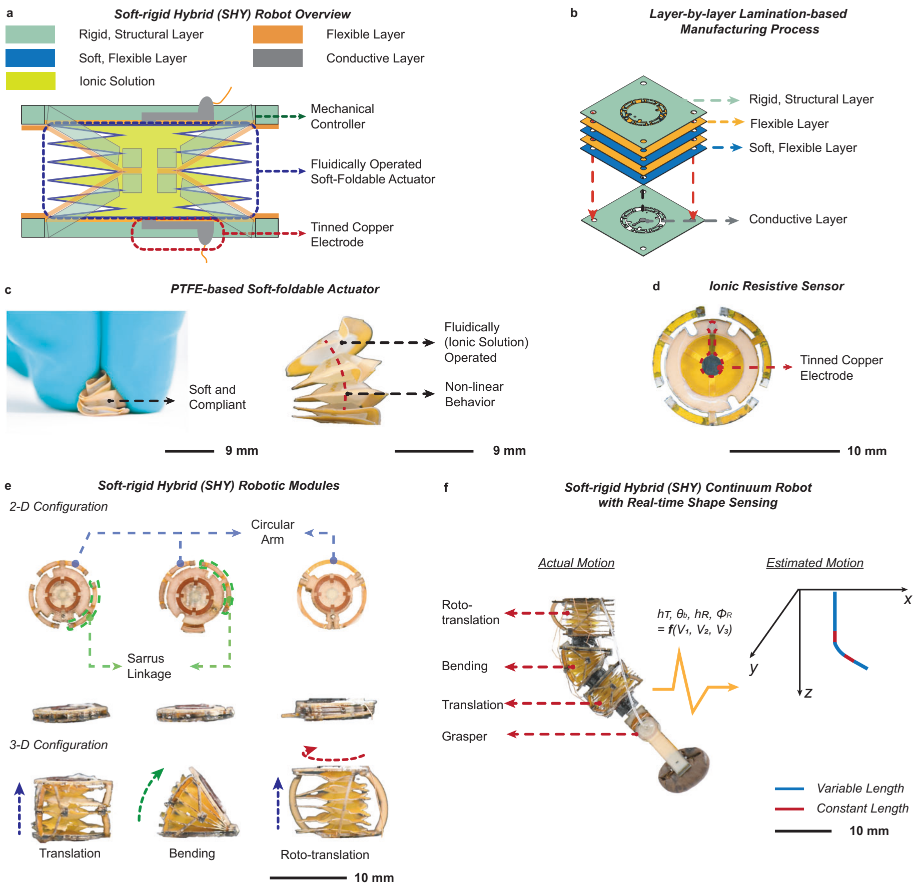

Fig. 1 | SHY robots overview. a A schematic illustration of a SHY robotic module. A SHY robotic module contains a mechanical controller, a PTFE soft-foldable actuator, and tinned copper electrodes to operate in an encoded manner and self-sense its motion. **b** SHY robotic modules are fabricated by laminating films with various properties (i.e., rigid, flexible, soft, and conductive) after hydrogen plasma surface treatment of PTFE films to promote adhesion. **c** A PTFE soft-foldable actuator is made of soft and compliant materials (left: the actuator can be squeezed with two fingers) and operated using an ionic solution, producing motion upon pressurization (right). **d** Tinned copper films are installed within the robot to embed an ionic resistive sensor. **e** 2-D (flat) and 3-D (expanded) configurations of SHY robotic modules. Three distinct types of mechanisms (translational, bending, and rotation with translational motion) encode the motion of SHY robotic modules. **f** A SHY continuum robot is constructed by stacking multiple SHY robotic modules. A grasper demonstrates an object manipulation task. The SHY continuum robot can sense its shape in real time using the embedded ionic resistive sensors. By reading voltages (V_1, V_2, V_3) from each sensor, the pose of corresponding modules (height, h_T, for a translational module, bending angle, θ_b, for a bending module, and height, h_R, and rotational angle, ϕ_R, for a roto-translational module) can be measured.

balloon, it generates motion by altering its curvature during inflation, forming a series of balloons and adopting a bellow-like configuration. The conversion from a 2-D to a 3-D bellow-like configuration is achieved by selectively bonding PTFE films, with attachment points on the films acting as hinges. As depicted in Fig. 1c and Supplementary Movie 1, the PTFE-based soft-foldable actuator exhibits softness and compliance resulting from both its constituent material and structural design. This allows it to readily conform to external loads. The motion of this PTFE-based soft-foldable actuator is characterized by non-linear behavior. Upon pressurization, the balloons buckle due to the inextensibility of the films, resulting in unpredictable bending in various directions, as illustrated in Fig. 1c.

To achieve controlled motion, the SHY robots incorporate a mechanical controller comprising rigid and flexible films. By suitably constraining soft-foldable actuators through pre-designed rigid linkages and flexible joints, the final kinematics of SHY robots can be encoded while still maintaining the structural compliance that provides their softness. Consequently, by integrating different mechanisms, the same soft-foldable actuators can manifest various types of motion. In this work, three different mechanism designs are introduced to produce three SHY robotic modules with translation, bending, and roto-translation degrees of freedom (DOFs), as shown in Fig. 1e.

Each of the proposed SHY robotic modules integrates an ionic resistive sensor (Fig. 1d). The sensor is realized by attaching electrodes on the internal surfaces of the actuator's top and bottom plates and electrically connecting the electrodes through an ionic solution made up of a mixture of sodium chloride and deionized water (Fig. 1a). As a result, the resistance across the electrodes changes as the fluid fills up the intermediate balloons, and this change is used to estimate the robot configuration.

The translational DOF (Fig. 1e) produces extending, linear motion as the embedded PTFE soft-foldable actuator (9 mm in OD balloons for 11.5 mm scale, 3 mm in OD balloons for 5 mm scale) expands. This is achieved by including multiple sets of Sarrus linkage, a mechanism that converts a limited angular linkage motion into a linear motion. The circular arms of Sarrus linkages are installed along the radius of the actuators to prevent the increase in diameter as they expand. The maximum extension of the translational DOF depends on the chord length of each circular arm and the maximum bending angle of flexible joints. As illustrated in Supplementary Fig. 1a, the maximum bending angle of the flexible joints can be controlled by adjusting the thickness of the rigid layers (t) and the gap between two rigid components (g) as indicated in Supplementary Equation (1). As a result of bending the circular arms, the total translational DOF range of motion is h_T (Supplementary Equation (2)), as shown in Supplementary Fig. 1b.

Similarly, the bending DOF (Fig. 1e) includes two sets of Sarrus linkage. In addition, on one side of the actuator, a constraining flexible joint is installed, forcing the actuator to bend around the constraining joint. Thus, the embedded PTFE soft-foldable actuator (9 mm in OD balloons for the 11.5 mm scale, 3 mm in OD balloons for the 5 mm scale) moves along an arc centered at the constraint. Like other flexible joints, the maximum bending angle of this constraint joint can be calculated using Supplementary Equation (1). In addition, the maximum bending angle of the actuator is constrained by the chord length of the circular arms (see Supplementary Information). As described in Supplementary Equation (3), shorter chord lengths of arms result in a smaller maximum bending angle by mechanically stopping the actuator from further bending. From a known angle of bending, the translation at the center of the mechanism can be derived (Supplementary Fig. 1c).

The roto-translational DOF (Fig. 1e) is achieved by connecting the top and bottom sides of the actuator with circular-shaped arms, resulting in interdependent rotation and translation movement. The bottom side of the PTFE soft-foldable actuator (6.7 mm in OD balloons for the 11.5 mm scale, 3 mm in OD balloons for the 5 mm scale) is not constrained such that it can freely rotate (ϕ_R) about the center axis (Supplementary Fig. 1d). Thus, as the balloons expand (h_R), the arms bend around the flexible joints and cause the top side of the actuator to rotate with respect to the bottom side (Supplementary Fig. 1e). The rotation that occurs during the expansion of balloons can be found using the kinematics shown in Supplementary Equation (8). As Supplementary Equation (8) describes, the movement of the actuator is limited by the arc length of the circular arms, which controls the height of the actuator.

SHY Robot manufacturing

The SHY robots are manufactured by laminating film materials in a layer-by-layer fashion after laser precision micromachining, H_2 plasma surface modification of PTFE, alignment, and stacking (Fig. 2, Supplementary Fig. 3, and Supplementary Movie 2). Robot constituent components include fiber-reinforced epoxy laminate as a rigid structural material, polyimide as a flexible material for robot joints, PTFE film as a soft and flexible material for soft actuator construction, copper as conductive material for sensing, and heat-activated acrylic sheet adhesive films for bonding. After laser machining films (Fig. 2a), paper-backed acrylic adhesive films are selectively peeled off to bond selected locations (Fig. 2b), copper films are tinned to prevent corrosion which can be induced by the ionic solution (Fig. 2c), and PTFE films are exposed to H_2 plasma chemical surface modification to promote adhesion (Fig. 2d).

H_2 plasma surface modification is necessary as PTFE possesses high chemical resistance due to stable carbon-fluorine bonds (Fig. 3a), preventing adhesion with other materials and the selected heat-sensitive adhesive film. As shown in Fig. 3a, the chemical composition of pristine PTFE films changes after plasma etching with H_2 gas (illustrated by purple zig-zag arrows). During the H_2 plasma treatment, hydrogen radicals begin to combine with fluorine atoms (depicted by red arrows). Consequently, fluorine atoms detach from the carbon-fluorine bonds (indicated by green arrows), forming hydrogen fluoride (HF) and leading to changes in the chemical properties of the PTFE films. This plasma etching process modifies the chemical properties of PTFE films, making them more hydrophilic and enhancing the bond between PTFE and adhesive films. This is demonstrated in Fig. 3b, where markings from a permanent marker minimally stay on a pristine PTFE film, but permanently stay on a H_2 plasma-etched PTFE film (Supplementary Movie 3).

The hydrophilic nature of the H_2 plasma-etched PTFE film is further confirmed by contact angle measurements, as shown in Fig. 3c. In Fig. 3c, a deionized water droplet is used as a probing liquid to measure the contact angle of the pristine and plasma-etched film using a contact angle goniometer (DSA100, Kruss Scientific). The plasma-etched PTFE film exhibits a lower contact angle(117.88°) compared to the pristine PTFE film (88.36°). This reduction in contact angle indicates an increase in surface energy, facilitating the bonding of adhesive films onto the plasma-etched PTFE films. Furthermore, to offer a more concrete perspective on the chemical modification of the PTFE film, we investigated the critical surface tension of PTFE films before and after our functionalization process. This involved using probing liquids with various surface tensions and measuring the contact angle of each probing liquid with the PTFE films (Supplementary Fig. 4a). These liquids included: deionized water (surface tension of 72.8 mN/m), glycerol (surface tension of 63.4 mN/m), ethylene glycol (surface tension of 48 mN/m), chlorobenzene (surface tension of 33.6 mN/m), and isopropanol (surface tension of 23 mN/m). Based on these measurements, the Zisman plot (Supplementary Fig. 4b) was generated to quantify the critical surface tension of the PTFE films before and after H_2 plasma surface modification (i.e., after one hour) and after a prolonged period of time post H_2 plasma treatment (i.e., after one week). As depicted in Supplementary Fig. 4b, and Supplementary Table 1, the Zisman plot illustrates that the plasma-etched PTFE film exhibits a higher critical surface tension (γ_c), indicating that liquids with higher surface tension can completely wet the plasma-etched PTFE film (Supplementary Fig. 4a). As demonstrated by the Zisman plot, this plasma surface modification is a permanent alteration process, independent of environmental conditions (i.e., temperature and humidity). The samples tested after one hour of H_2 plasma surface modification and after one week retained the same surface energy. This facilitates time-independent permanent bonding of PTFE with adhesive films (i.e., once the film samples have been treated with H_2 plasma, they can be stored and bonded at any time). As shown in Supplementary Fig. 5 and Supplementary Table 2, it was found that 450 W etching power and 5 min etching time resulted in the highest adhesive strength of PTFE films (0.220 N/mm) from peeling tests carried out with the ASTM D1876 standard (see Supplementary Information).

To embed sensing capabilities in the SHY robotic modules, tinned copper conductive traces are integrated and permanently bonded to the top and bottom layers of the modules (Figs. 1a, 2e–g). Subsequently, all the layers of the robot are aligned, stacked, and bonded together (Fig. 2h, i) by heat pressing. The SHY robot is then released from the scaffold by laser cutting (Fig. 2j). Finally, necessary inlet tubing and wires are installed by using UV adhesive (< 10 s to cure) and soldering (Fig. 2k).

Range of motion

The range of motion of the 11.5 mm OD SHY robotic modules was characterized by hydraulically pressurizing the PTFE soft-foldable actuator at a constant flow rate, 0.1 ml/min (see Supplementary Information and Supplementary Fig. 2 for the range of motion of 5 mm OD SHY robotic modules). Upon pressurization from 0 kPa to 140 kPa, the robots transform from a ≈ 2-D to a 3-D shape, making translational (Fig. 4a), bending (Fig. 4b), and roto-translational (Fig. 4c, d) motions. In the fabricated SHY robotic modules, the translational and bending modules comprise five pouches of PTFE balloons and the roto-translational module contains six pouches of PTFE balloons. During the experiment, a magnetic tracker system (NDI Aurora) was used to measure the range of motion with the attached probe at the top surface of each robot.

As indicated in Fig. 4a, the maximum extension of the translational robotic module is 5.2 mm ± 0.2 mm. The maximum bending angle of the bending module is 50.9° ± 2.96° (Fig. 4b). The maximum extension and twisting angle of the roto-translational module are 5.05 mm ± 0.25 mm (Fig. 4c) and 39.4° ± 1.3° (Fig. 4d), respectively. As shown in Fig. 4a, b, the range of motion of the translational and bending module starts to plateau around 140 kPa because the encompassing rigid-flexible mechanical controllers mechanically

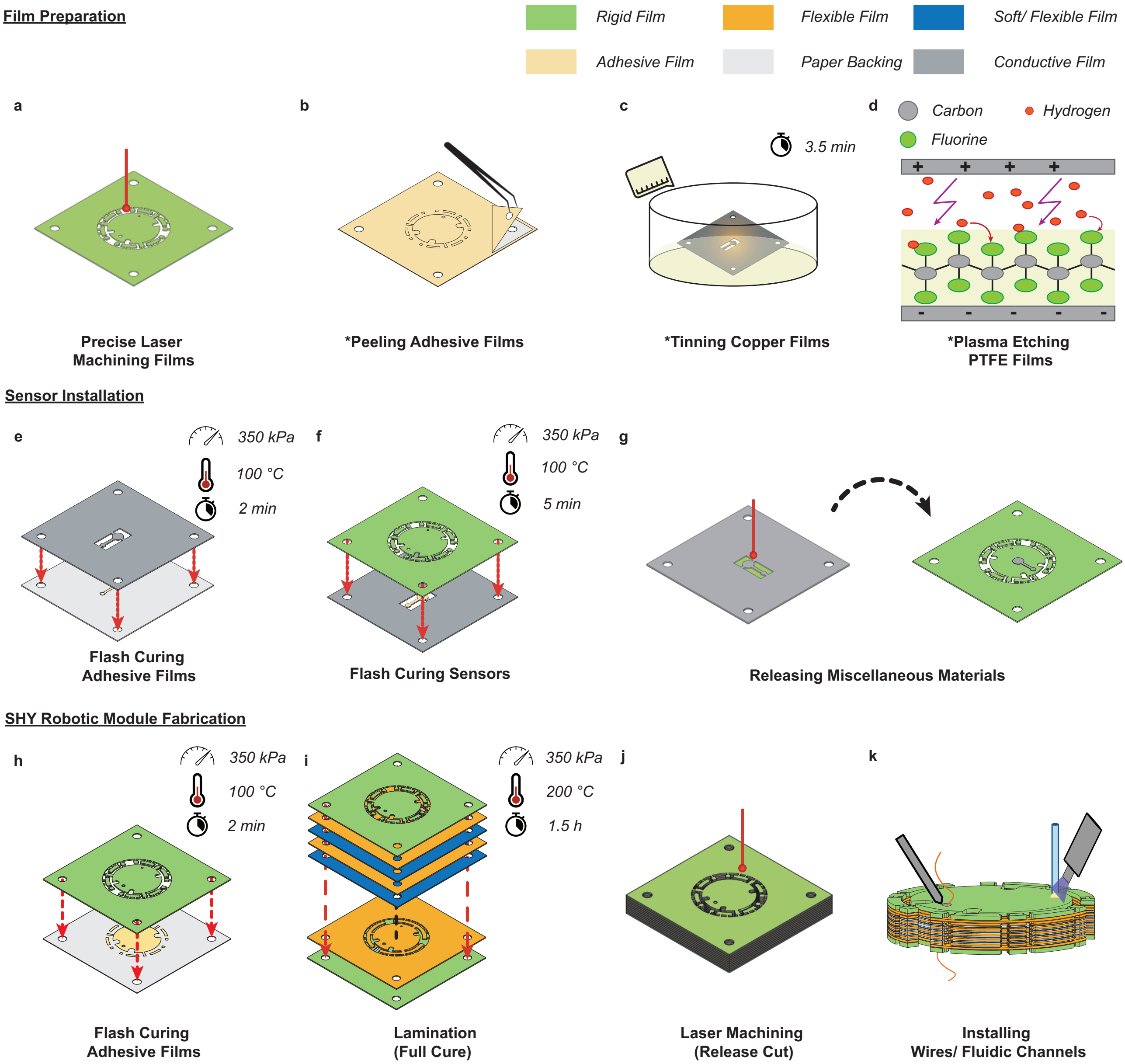

Fig. 2 | Fabrication process of SHY robots. a Films are precisely cut using a laser precision micromachining workstation. **b** Adhesive films are peeled off to selectively bond films. **c** Copper films are tinned using a tinning solution to prevent corrosion of films. **d** PTFE films are plasma etched to promote the bonding of adhesive films. **e** An adhesive film is cured shortly to transfer to a tinned copper film. **f** The tinned copper films are temporarily attached to structural layers by heat pressing for 2 min. **g** Excess copper material is removed via laser cutting. **h** All the adhesive films are transferred to other films by curing for 2 min. **i** All the films are precisely aligned using dowel pins and stacked in order. Films are cured for 1.5 hours to permanently bond. **j** The robot is removed from the scaffold by laser machining. **k** Necessary wires and fluidic channels are installed. * symbol indicates procedures that can be done in parallel.

stop them from further expansion. These results closely matched the geometrical model (see Supplementary Information) of the translational and bending module, indicating that the maximum range of motion can be mechanically encoded during the design phase. On the other hand, in Fig. 4c, d, the range of motion of the roto-translational module does not plateau around 140 kPa. This suggests that more balloons can be added within the PTFE soft-foldable actuator to reach the maximum range of motion. As represented in the geometrical model, the predicted maximum range of motion of the roto-translational module is about 1.7 mm and 50° greater than the experimented values. Yet, as indicated in Supplementary Fig. 6a, the actual motion observed in the roto-translational module prototypes consistently followed the motion predicted by the geometric modeling. This geometric model can effectively predict both the rotational motion based on the extension and vice versa. The maximum error observed between the experimentally measured and geometrically predicted rotational angles, given the extending motion as an input, is 9 %.

Output force and torque performance

Output force and torque performance characterizations for each of the 11.5 mm OD SHY robotic modules are shown in Fig. 4e–h (see Supplementary Information and Supplementary Fig. 2 for the output force and torque performance of 5 mm OD SHY robotic modules). The orientation and the initial distance between the force/torque (F/T) sensor and the robot were adjusted at different expansion states of the PTFE soft-foldable actuator (i.e., 0% expansion, 25% expansion, 50% expansion, and 75% expansion with respect to the maximum actuator

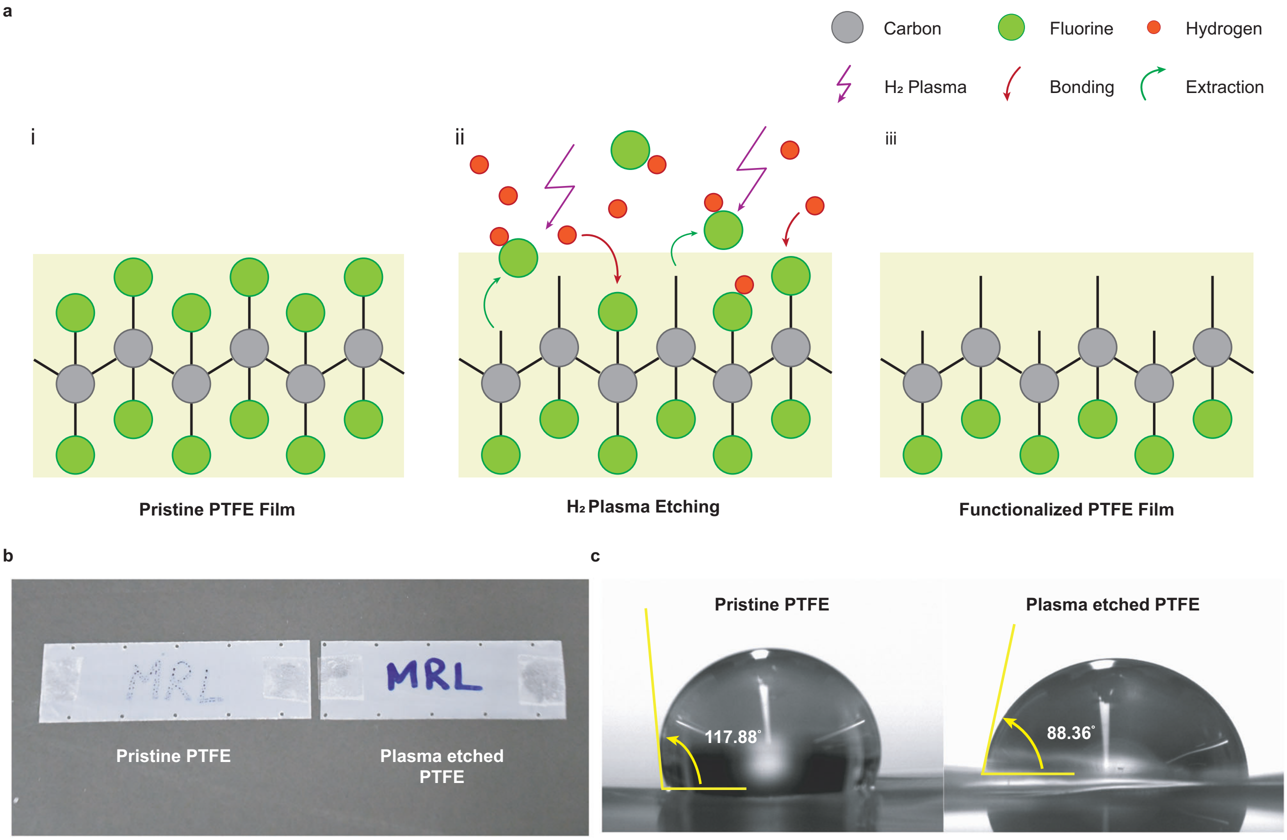

Fig. 3 | Altering properties of PTFE films using hydrogen plasma. a A schematic illustration of the hydrogen plasma etching process. (i) Pristine PTFE films contain stable carbon-fluorine bonds, providing high chemical resistance. (ii) Hydrogen gas (H_2) is used as a process gas to extract fluorine atoms from the carbon-fluorine bond. (iii) The functionalized PTFE films have unsaturated carbon compounds, allowing adhesive films to bond to PTFE films. **b** Markings from a permanent marker minimally stayed on a pristine PTFE film. Markings permanently stay on a plasma-etched film (Supplementary Movie 3). **c** Contact angle measurement of the pristine and plasma-etched films using deionized water as a probing liquid. The plasma etching process decreases the contact angle of the PTFE film, chemically modifying the surface.

expansion) to capture the output force and torque in various conditions. The results show that the maximum output force that translational, bending, and roto-translational modules can generate are 4.44 N ± 0.02 N (Fig. 4e), 3.36 N ± 0.12 N (Fig. 4f), and 3.78 N ± 0.02 N (Fig. 4g), respectively.

Here, we estimated the maximum output force of each actuator using the simple linear relation $F = P * A$, where F is output force, P is input pressure, and A is the cross-sectional area of the PTFE soft-foldable actuator. As indicated in a dashed line in Fig. 4, the output force model exhibits a close correlation with the actual output force of the translational, bending, and roto-translational modules, with max errors of 1.5%, 7%, and 3.5% respectively.

In addition, the results indicate that restraining the actuator at a more extended position, influenced by the external constraint's location, leads to a reduction in the generated output force. These results can be explained using the principle of virtual work, where virtual work done by an external force needs to be equal to virtual work done by internal pressure. This can be expressed as

$$F = P\frac{d\forall}{dh} \tag{1}$$

where F is an external force, P is internal pressure, $d\,\forall$ is the change in volume, and dh is the change in height. As illustrated in Supplementary Fig. 7, in the further expanded condition, the output force would be less since the work done by the internal pressure is constant but the change in height of the actuator is increased. Thus, this would effectively reduce the magnitude of output force.

Similarly, the virtual work principle can be utilized to calculate the output torque that can be exerted by the roto-translational module. Assuming that the work done by the internal pressure is used to either produce purely output force or torque, the maximum output torque can be calculated (see Supplementary Information for a detailed derivation):

$$T = F\frac{dh}{d\phi} \tag{2}$$

where T is the output torque, F is the output force, and $dh/d\phi$ is the kinematic coefficient of the current expansion state of the actuator. With this calculation, the maximum output torque of the roto-translational module is 84.89 Nmm ± 0.77 Nmm (Fig. 4h). It is worth noting that, as represented in Equation (2), the output torque depends not solely on the output force but also on the expanded configuration of the module. Thus, as highlighted in Fig. 4g, h and Supplementary Fig. 6b, high output torques are achieved at less expanded configurations due to the combined effects of high output force and a high kinematic coefficient.

Power density

The maximum power density in the 11.5 mm SHY robotic modules was estimated using the measured data for mass (0.18 g), speed, and force (see Supplementary Table 3). Then, the following equation was applied

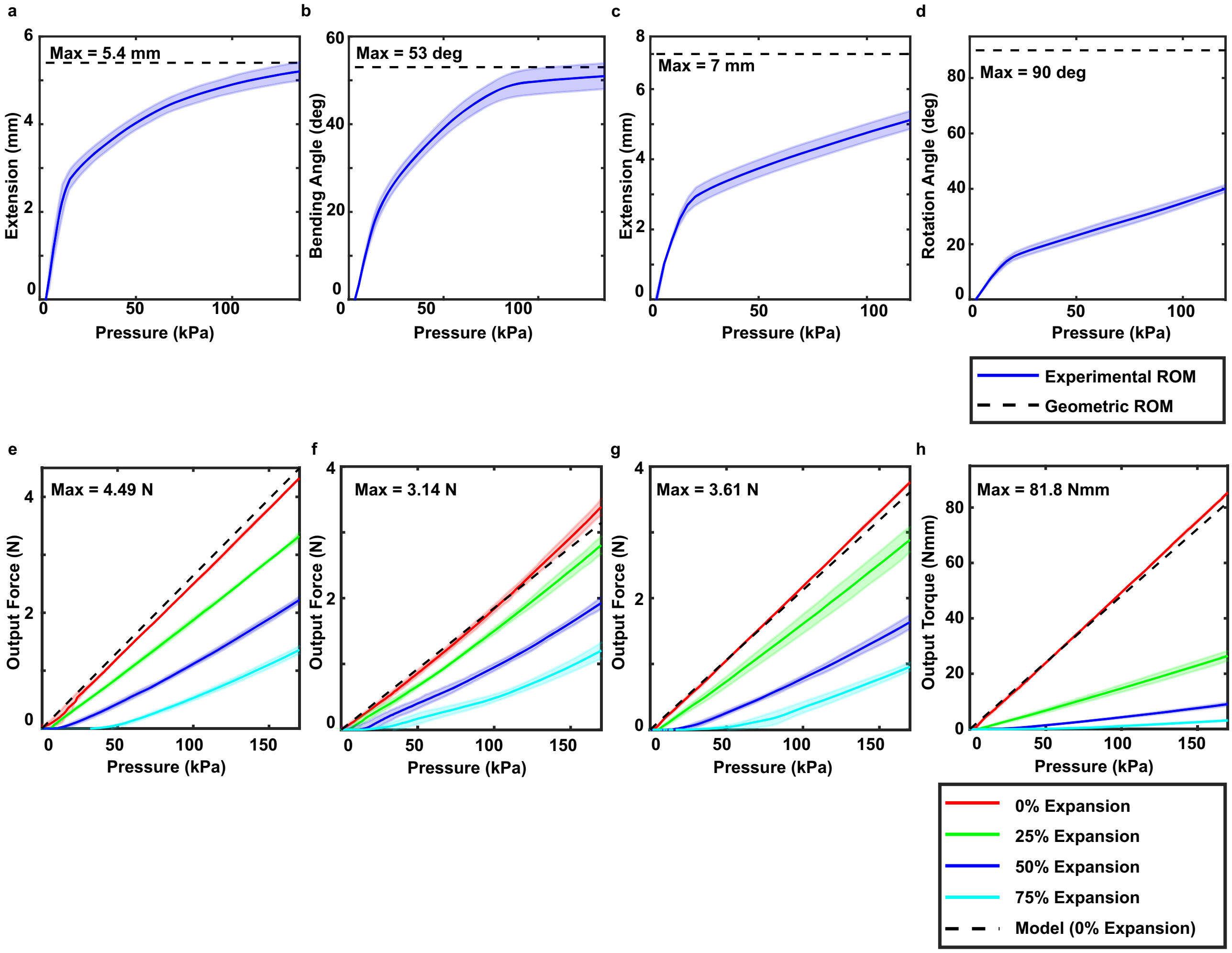

Fig. 4 | Mechanical Characterization of SHY robotic modules. Experimental results of range of motion of (**a**) translational, (**b**) bending, and (**c**, **d**) roto-translational modules, and corresponding geometric calculation. Output force performance of (**e**) translational, (**f**) bending, and (**g**) roto-translational modules in various expansion states. **h** Output torque performance of roto-translational modules in various expansion states. The solid line is the mean resulting from three experiments on three prototypes, and the shaded area is the standard deviation. The dashed line is the output from the theoretical model, where the corresponding theoretical maximum is indicated on the plot.

to calculate the power density P_D:

$$P_D = \frac{Fv}{m} \tag{3}$$

where F is the maximum output force, v is the maximum output speed, and m is the mass of an actuator. For the bending module, the output torque was calculated by multiplying the output force by the moment arm (r), the distance between the center of the actuator and the constraint joint. The maximum speed of the translational and roto-translational modules was 4.48 mm/s and 4.14 mm/s, and the maximum angular speed of the bending module was 2.80 rad/s. Using the measured data, the maximum power density, ρ, of the translational, bending, and roto-translational modules resulted in 110.41, 52.30, and 86.99 Wkg^{-1}, respectively.

Sensor model and characterization

An ionic resistive sensing mode is implemented in the SHY robotic modules (Supplementary Movie 4). The working fluid, an ionic solution made up of a mixture of sodium chloride and deionized water, electrically connects two electrodes positioned at the top and bottom of the robotic modules and works both as an actuation and sensing medium (Fig. 5a). The ionic solution utilized consists of a sodium-to-deionized water ratio of 1:10,000. The resistivity of the ionic solution was measured experimentally using a voltage divider circuit. The voltage divider circuit included a shunt resistor with a known resistance and an ionic solution-based resistor, which has a known cylindrical volume dimension. By applying Pouillet's law ($R = \rho L/A$), where R is the resistance, ρ is the resistivity, L is the length, and A is the cross-sectional area, the resistivity of the ionic solution-based resistor was calculated. This calculation resulted in a resistivity value of 180,791 Ω·mm.

After determining the resistivity of the ionic solution, the resistance of the ionic resistive sensor can be derived using Pouillet's Law, $R = \rho L_{eff}/A$, where length (L_{eff}) is the distance between electrodes (Fig. 5a). An ionic liquid with a high resistivity is desirable to create a large change in resistance with a small change in the volume of the ionic liquid. Pouillet's Law assumes that the resistor has a constant cross-sectional area. However, the soft-foldable actuators embedded in our robots have a bellows design, resulting in varying cross-sectional areas. As the balloons within the modules inflate, the plate area effectively increases, since more fluid expands outward into the bellows, making the area of the approximated cylinder larger. Addressing these effects, we introduce a corrective multiplicative function (K) into the model that considers the varying circular cross-sectional area. The variable cross-sectional area can be calculated as $A = \pi(Kr)^2$, where r is

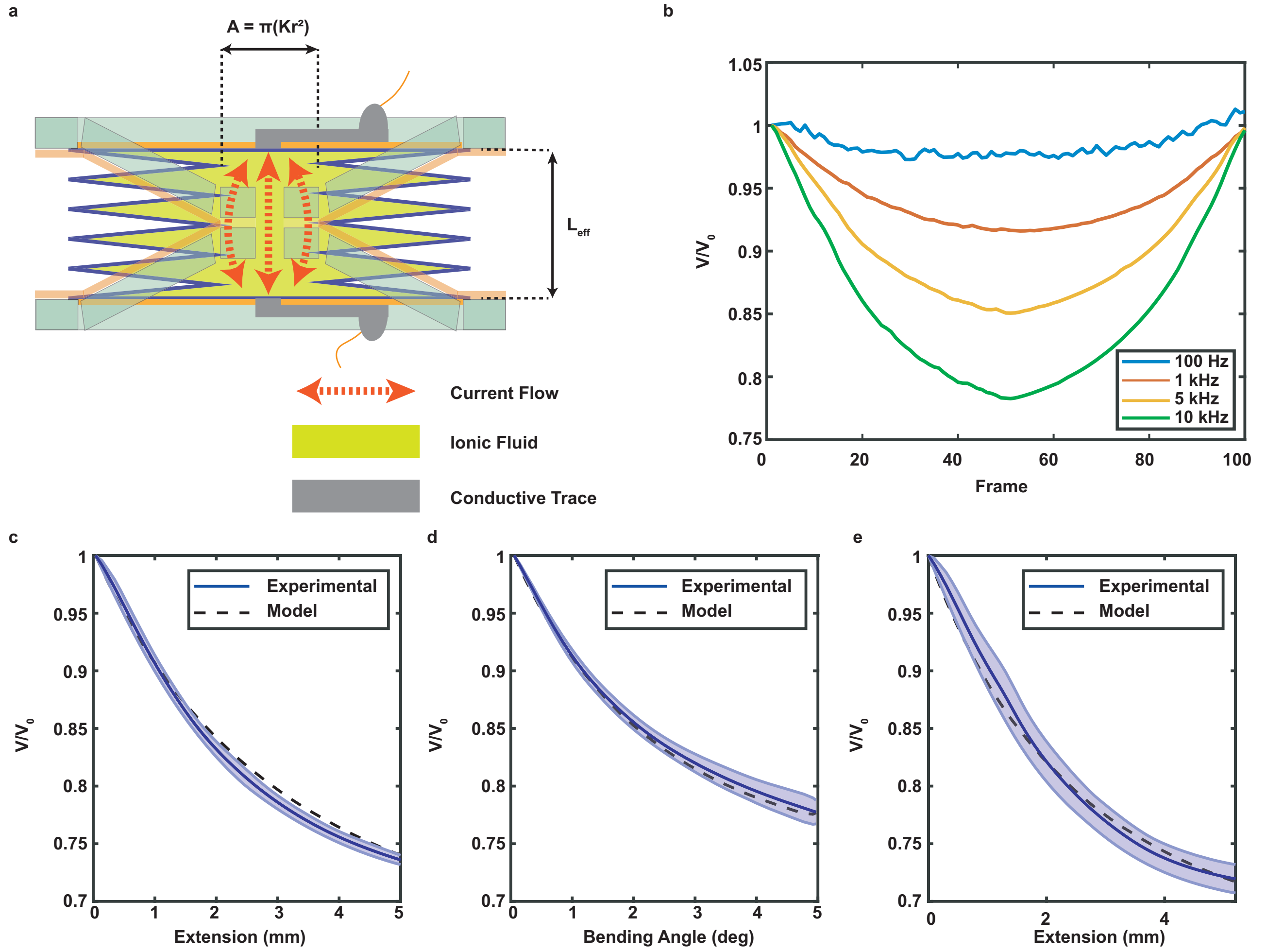

Fig. 5 | Sensor modeling and characterization. a The resistance across the embedded electrodes is varied as length (L_{eff}) increases. To account for the variable cross-sectional area of the soft-foldable actuator, a corrective multiplicative function, K, is applied to the radius of the electrode, r. AC current flows across the electrodes to prevent polarization of ionic solution. The conductive traces are electrical pathways formed using tinned copper films. In SHY robots, these conductive traces are employed to create the electrodes of the ionic resistive sensor. **b** Comparison of various input frequencies. Measured normalized voltage (V/V_0) as (**c**) translational, (**d**) bending, and (**e**) roto-translational SHY robotic modules (11.5 mm OD) are actuated. In (**c**), (**d**), and (**e**), the solid line is the mean resulting from three experiments on three prototypes, and the shaded area is the standard deviation. The dashed line is the output from the sensor model.

the radius of the electrode and K is a corrective multiplicative function that takes into account the irregular geometry of the PTFE soft-foldable actuator. The term acts as a multiplicative function K on the electrode radius by increasing linearly as the actuator expands.

To examine the sensor performance, the voltage across the robotic modules was measured as they expanded. This was achieved using a low-voltage, high-frequency sine wave as the power source for several reasons. A sufficiently high-frequency input wave is required for ionic resistive applications to reduce the effect of capacitance impedance and prevent polarizing ions to one side of the sensor. Previous works have utilized frequencies above 1 kHz for similar ionic resistive applications[33,34]. A frequency of 10 kHz was chosen based on experimental results on prototypes tested at various frequencies ranging from 100 Hz to 10 kHz. As shown in Fig. 5b, 10 kHz frequency provides the largest variation in the root-mean-square (RMS) voltage upon the robot's movement. In addition, low voltage, 1 V peak-to-peak voltage, was used to prevent the corrosion of tinned copper films and inhibit the electrolysis of water, where the water breaks up into hydrogen and oxygen gas at 1.5 V[64]. Thus, a 1 V peak-to-peak, 10 kHz sine wave was chosen as the power source in this work. As shown in Supplementary Fig. 9, the sensor was placed in series with a 680 kΩ shunt resistor to form a voltage-dividing circuit, where it acts as a variable resistor. The output voltage (V) was measured across the shunt resistor using an RMS voltage sensor (LTC1968, Analog Devices), which calculates the RMS values of an AC signal and outputs them as DC voltages in real time. The output voltages (V) were then normalized using the initial baseline voltages (V_0).

Figure 5 c shows the normalized voltage (V/V_0) across the sensor versus the extension for the translational SHY robotic module (11.5 mm OD). The sensor is able to map across the entire range from 0 to 5 mm range of linear extension. Figure 5d shows the normalized voltage across the sensor versus the bending angle for the bending SHY robotic module (11.5 mm OD). Again, the sensor is able to map across the entire 0 to 50° range of bending. Finally, the result for the roto-translational SHY robotic module (11.5 mm OD) is shown in Fig. 5e, with the embedded sensor mapping across the full deflection range of 0 to 5 mm of extension. The coupled rotating motion, ranging from 0 to 40° of rotation, can be computed using geometric modeling (Supplementary Fig. 6a). The max standard deviation for the sensors was found to be 0.0068, 0.0178, and 0.0219 (see Supplementary Table 4). Similarly, it was possible to integrate the ionic resistive sensor into the 5 mm OD SHY robotic modules (See Supplementary Information and Supplementary Fig. 2). For both scales of SHY robotic modules, they exhibit a nonlinear, monotonic response, meaning this sensing modality could be utilized for the sensor feedback for the robot position control.

SHY Continuum robot design

We built a soft-rigid hybrid continuum robot by combining multiple SHY robotic modules in series with fixed spacers in between. A notable design feature of the SHY continuum robot is the integration and routing of fluidic inlet channels via lateral passage holes. Fluidic inlet channels and sensor wires are positioned off-center in the SHY robotic modules (Supplementary Fig. 10) so that they can pass through the connected modules without obstructing or interfering with the actuation and sensing abilities of multiple modules. This enables the fabrication of numerous combinations of multi-DOF continuum robots by stacking various modules. The fluidic inlet channel for the roto-translational SHY robotic module is fixed at its base in the center to avoid excessive torsion on the tubing. Thus, this robotic module can be positioned at the base of the continuum robot. Supplementary Fig. 10 illustrates one possible combination of SHY robotic modules in a 3-DOF continuum robot, constructed by stacking in order a roto-translational, a bending, and a translational module (i.e., R-B-T configuration).

Real-time shape sensing of SHY continuum robot

We demonstrated real-time shape-sensing of the SHY continuum robot (in the R-B-T configuration) by moving the system within its workspace and estimating the deflection of each module (using the embedded ionic resistive sensors). In a SHY continuum robot system, each SHY module's pose relies on the preceding SHY modules, similar to how the joints of a rigid robotic arm depend on preceding joint movements. Thus, using the proposed ionic resistive sensor and knowing the initial thickness of each robotic module (i.e., when flat, non-actuated), the forward kinematics can be computed.

With these dependencies, tracked points along the robot can be predicted, including the tip position and shape of the continuum robot (see Supplementary Information). Figure 6a shows the proposed SHY continuum robot in various configurations and demonstrates the estimated shapes of the robot using the embedded ionic sensor. Figure 6a presents the first actuation sequence of three sequences shown in Supplementary Movie 5. The robot actuates modules into the following configurations: (i) flat state, (ii) fully expanded roto-translational module, (iii) fully expanded bending and roto-translational module, (iv) fully expanded continuum robot, (v) fully expanded translational and bending module, and (vi) fully expanded translational module. The actual tip position of the continuum robot was measured using a magnetic tracker system (NDI Aurora), represented as a green dot in Fig. 6a. Figure 6b shows the relative error between the actual and predicted tip position and the length of the continuum robot for all three actuation sequences shown in Supplementary Movie 5. During this experiment, the average error between the actual and predicted configuration space was found to be 1.133 mm, demonstrating that the shape-sensing and tip-tracking of the continuum robot in 3-D space were functional.

SHY Continuum robot demonstration

Hereafter, we demonstrate the potential applications of the proposed robotic technology. The SHY continuum robot is integrated with various end effectors, including a robotic grasper, a needle, and an optical fiber. The integration of a robotic grasper enables pick-and-place tasks, showcasing potential applications in food handling, manufacturing, and surgery. The addition of a needle and an optical fiber demonstrates potential applicability in medical procedures (e.g., tissue biopsies and laser ablation).

Showing object manipulation with the SHY continuum robot, we integrated a robotic grasper (Supplementary Fig. 11) onto the SHY continuum robot and performed pick-and-place tasks of soft and hard objects of various shapes, sizes, and weights (Fig. 7 and Supplementary Movie 6) using open-loop control. The grasper was manufactured using the same manufacturing technique (Supplementary Fig. 11a) described in this paper and featured embedded PTFE soft-foldable actuators (4 mm OD) to facilitate jaw opening and closing, via the application of positive and negative pressure (Supplementary Fig 11b). Upon pressurizing up to 140 kPa, the subtended angle of grasper jaws can increase up to 40° (Supplementary Fig. 11c). Conversely, as shown in Supplementary Fig. 11d, the grasper can exert up to a maximum grasping force of 180 mN by pulling a vacuum pressure of -100 kPa. The grasper was attached to the SHY continuum robot's tip using UV adhesive.

The robot was positioned in a test setup where it hung from a top surface and interacted with objects on a lower surface. The grasped objects included small food items (Fig. 7a–h), assembly and fabrication components (Fig. 7i), daily objects (Fig. 7j, k), and a 50 g weight (Fig. 7l). The robot successfully grasped and moved an average distance of 20 mm for each object. As Fig. 7 depicts, the robot performed pick-and-place tasks for all objects included in our test, from smaller objects (i.e., a black rice grain (Fig. 7a), a coffee bean (Fig. 7b), a pomegranate seed (Fig. 7c), a Gummy bear (Fig. 7d), an M6 nut (Fig. 7i), and a LEGO block (Fig. 7j)) to relatively larger objects like an 18 × 20 × 5 mm letter block from the Scramble Game (Fig. 7k), exceeding the size of the grasper (17 × 3 × 1.7 mm). Of these objects, the smallest grasped item was a black rice grain with a width of 2 mm. In addition, the robot was able to manipulate delicate, soft food items (i.e., a tangerine vesicle (Fig. 7e), a blueberry (Fig. 7f), a salmon roe (Fig. 7g), and a raspberry (Fig. 7h) without damaging the grasped objects. Figure 7l illustrates that the robot, which has a total weight of 2 g, was capable of lifting a 50 g weight that is 25 times heavier than the robot itself.

To showcase robotic needle steering, a 30-gauge needle with a 304 µm inner diameter (ID) microtubing (MRE025, Braintree Scientific, Inc.) was integrated onto the tip of the SHY continuum robot and fixed using UV adhesive. Simulating medical biopsy and drug delivery procedures, we tested the system on an in vitro tissue simulator, featuring four target locations marked with circular rings. Utilizing open-loop control, the robot navigated toward each of the four targets, steered the needle end-effector as needed, deployed the needle into the tissue analog, and performed penetration, and pink dye, representing a drug solution, was injected. As depicted in Fig. 8a and Supplementary Movie 7, the SHY continuum robot exerted sufficient force to penetrate the tissue simulator, and the injection of pink dye validated this process. This capability holds promise for various medical applications, including drug delivery and tissue biopsy in minimally invasive surgical procedures. In these applications, the robot needs to be able to accurately guide the end effector and apply sufficient force in the desired direction to penetrate tissue to perform tasks such as taking tissue biopsy or delivering drugs.

To demonstrate optical fiber steering capabilities for potential applications in medical procedures (i.e., laser ablation), an optical fiber (220 µm) was securely attached to the tip of the SHY robot using UV adhesive. In this demonstration, we utilized green LED light to simulate laser light. The SHY continuum robot was positioned upside down and maneuvered toward the targets indicated by the brown rings (see Fig. 8b and Supplementary Movie 8).

Similar to the divergence of laser light upon exiting the optical fiber, the green LED light also diverges as it exits the optical fiber. This dispersion reduces the light's focus, lowering its ability to deliver concentrated power to the target. Consequently, positioning the optical fiber closer to the targets becomes necessary to achieve focused and high-power light delivery. During actual laser-assisted surgeries, a larger laser spot size can inadvertently result in photothermal energy to unintended areas, potentially damaging healthy tissues[65]. Moreover, anatomical surfaces are rarely flat, necessitating constant control over the distance between the optical fiber and the target tissue to maintain a consistent laser spot size.

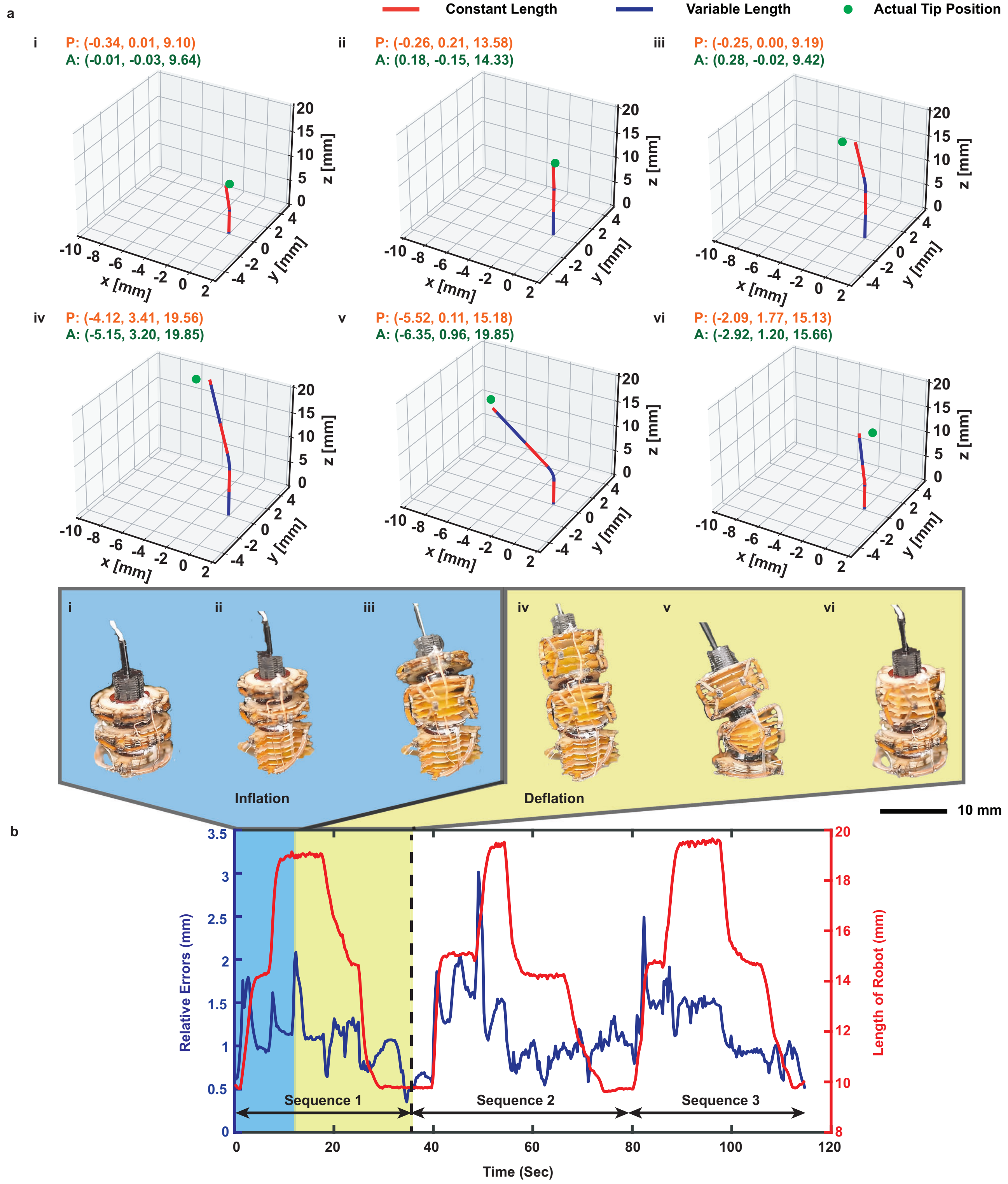

Fig. 6 | SHY continuum robot with real-time shape sensing. a Comparison of predicted (P) and actual (A) tip position of the SHY continuum robot for actuation sequence 1 shown in Supplementary Movie 5. The continuum robot initiates its sequence from the (i) flat state. Subsequently, the robotic modules undergo actuation in the following order: (ii) roto-translation, (iii) bending, and (iv) translation. The robotic modules are then retracted in the following order: (v) roto-translation, (vi) bending, and (i) translation. Green dots represent the actual tip position. Red links represent links with fixed heights and blue links represent links with various heights. **b** The relative errors between actual and predicted tip positions increase as the length of the robot increases. The relative errors and the length of the robot are for all three actuation sequences shown in Supplementary Movie 5.

As shown in Fig. 8b, the light is initially unfocused due to the long distance between the fiber and the targets, resulting in lower intensity. The optical fiber must be positioned closer to the target locations to achieve focused and high-power light delivery. We demonstrated this by moving the optical fiber toward three target locations. As shown in Supplementary Movie 8, the LED light was deactivated during movement and reactivated once the SHY continuum robot successfully aligned the optical fiber with the targets.

Fig. 7 | SHY robotic manipulator performing pick-and-place tasks. Objects (soft and hard) included in the pick-and-place test are as follows. **a** A black rice grain. **b** A coffee bean. **c** A pomegranate seed. **a**–**c** demonstrate the robot can manipulate small objects. **d** A gummy bear. **e** A tangerine vesicle. **f** A blueberry. **g** A salmon roe. **h** A raspberry. **d**–**h** demonstrates the robot can delicately grasp and move soft objects. **i** An M6 Nut. **j** A LEGO block. **k** A letter block. **l** 50 g Weight. **i**–**l** Demonstrate the robot can lift and move objects that are larger than its grasper and heavier than its own weight.

This simulates laser ablation, where laser light is applied only at the target locations to avoid undesired photothermal damage to healthy tissues. As depicted in Fig. 8b, the diameter of the light beam reduces as the optical fiber approaches the targets, indicating enhanced focus. This capability holds promise for applications in laser-assisted surgery, where precise control over the position of the optical fiber is crucial for the successful delivery of focused laser light and bloodless tissue ablation[65].

Discussion

We have introduced a manufacturing method for millimeter-scale SHY robots enabled by chemical surface modification of soft PTFE films via

https://doi.org/10.1038/s41467-024-51137-8

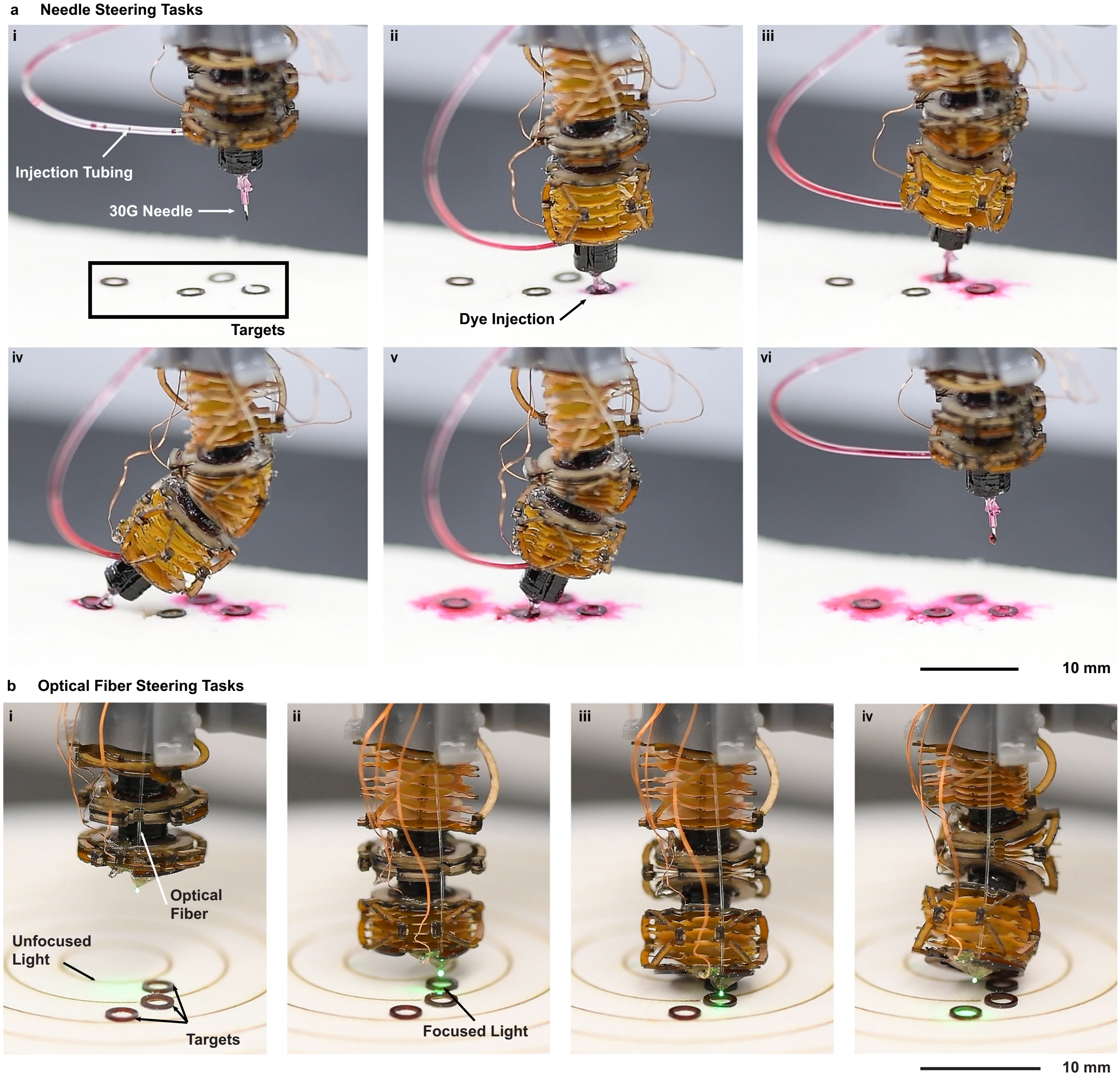

Fig. 8 | SHY continuum robot performing needle and optical fiber steering tasks. a The SHY continuum robot (i) successfully guides the needle toward four target locations (marked with black circular rings) on the tissue simulator. This in vitro experiment demonstrates robot needle steering and puncturing capabilities. After puncturing each target location, red dye is injected into the tissue analog to confirm puncturing (ii–vi). The SHY continuum robot is retracted back to its original position after successful injections. **b** The SHY continuum robot steers the optical fiber toward three brown ring targets. Initially, the LED light emitted through the optical fiber is unfocused (i) because of the considerable distance between the fiber tip and the targets. Once the robot reaches the targets, it successfully delivers focused light precisely, demonstrating its ability to deliver light therapy in different locations (ii–iv).

H_2 plasma. Although H_2 plasma etching of PTFE films has found applications as a coating layer in various fields, including space, biotechnology, and microelectronic packaging[66], this has not been applied in creating soft robots using plasma-etched PTFE films. The introduction of PTFE films for soft robot manufacturing paves the way for their operation within harsh environments characterized by high temperatures, humidity, and chemical exposure, such as medical sterilization. Providing thermal and chemical durability surpassing that of other soft films, PTFE films can withstand such environmental conditions. They are capable of withstanding temperatures exceeding 327 °C and remain insoluble in most chemicals and solvents. In addition, unlike bonding silicone films (e.g., PDMS bonding via oxygen plasma) and thermoplastic films, where the success of bonding is influenced by factors such as time, temperature, humidity, and cleanliness, the PTFE film bonding is not sensitive to these ambient conditions and time constraints.

In this work, we successfully achieved seamless integration of actuation, sensing, and mechanical control components within the robot materials using laser precision micromachining, chemical surface modification, and lamination, with minimal manual assembly steps. Demonstrating the versatility of the proposed fabrication method, we designed three distinct DOF SHY robotic modules (i.e., translational, bending, and roto-translational) and one DOF SHY robotic gripper. These constitute the building blocks of a robotic system, providing flexibility and different opportunities in designing and building full robotic systems, which can be tailored toward specific applications and needs, with our approach. Each robotic module exhibits unique degrees of freedom, which are mechanically encoded by an exoskeleton-like mechanical structure. Leveraging the capability for monolithic on-board integration of electrical circuits, we have seamlessly integrated an ionic resistive sensor into the SHY robots. This sensor is embedded by installing electrodes within the robots and utilizing an ionic fluid as a sensing medium. By fabricating SHY robotic modules at two different scales (5 mm and 11.5 mm OD), we demonstrated the scalability of this fabrication technology and the possibility of consistently manufacturing millimeter-scale soft robots by minimizing manual assembly procedures. Moreover, as highlighted in Supplementary Fig. 12, we demonstrated the feasibility of batch fabrication by incorporating a total of 15 modules within a single manufacturing session (see Supplementary Information). The DPSS laser precision micromachining system utilized in our manufacturing process has a working area of 15 × 15 cm. Therefore, up to ≈105 scaled-down (5 mm OD) SHY robotic modules can be manufactured in a single batch, if desired.

We have characterized the reliability of the proposed fabrication method with surface characterizations (i.e., contact angle measurements) to verify the successful chemical surface modification of PTFE films, and by testing the peel strength between PTFE films and our selected adhesive material. We have performed extensive mechanical characterizations of each SHY robotic module, including range of motion, force and torque, power density, and fatigue testing. We have embedded an ionic resistive sensor within the SHY robotic modules to self-sense the encoded motion by measuring the change in resistance across the robot's body. The ionic resistive sensors exhibit nonlinear behavior, but they do not display hysteresis as their measurements rely solely on the expansion state of the SHY robotic modules (i.e., the distance between the bottom and top conductive plates), not on the internal pressure. Furthermore, the ionic resistive sensor utilizes a low-voltage (1 V) AC signal and a biocompatible sensing medium to monitor the configuration of each module. This not only offers a safe sensing solution but also broadens the range of potential applications, such as minimally invasive surgery and drug delivery.

Our SHY robotic modules were designed to facilitate easy stacking in series, allowing for the creation of a continuum robot. Each SHY robotic module used in the SHY continuum robot has a diameter of 11.5 mm, lies in a flat state of around 1.7 mm in height, and possesses minimum features in the micrometer scale. As demonstrated in this paper, we incorporated a side-inlet channel design and guidance slots to effectively route fluidic lines and sensing lines throughout the robot. These features ensure proper alignment of fluidic channels and wires, minimizing interference. In addition, the dedicated fluidic channels enabled the simultaneous activation of multiple modules, facilitating complex and coordinated movements in the SHY continuum robot. Combining these modules in series, we successfully fabricated a proprioceptive SHY continuum robot and demonstrated real-time shape-sensing functionality through the use of integrated ionic resistive sensors. While this paper showcases the construction of a continuum robot using a specific combination (i.e., the aforementioned R-B-T configuration) of SHY robotic modules, it is important to note that various other combinations are possible. These combinations can be chosen based on the desired robot's kinematics.

As highlighted in this paper, various end effectors, including a grasper, a needle, and an optical fiber, can be compactly integrated. Using these end effectors, we showcased practical applications of the SHY continuum robot executing various tasks, i.e., object pick-and-place, needle steering and tissue puncturing, and optical fiber steering tasks. The pick-and-place task was achieved by integrating a grasper, fabricated using the same manufacturing technique. The robot was able to complete this task with soft and hard objects of various shapes and sizes, including small food items (a rice grain and a coffee bean), assembly and fabrication components (a nut), daily objects (a LEGO block and a letter block from the Scramble Game), and a 50 g weight (25 times heavier than the robot itself). This demonstrates the potential of the developed SHY continuum robot manipulator in real-world scenarios. The needle steering and tissue puncturing task was demonstrated by integrating a needle into the robot and steering it toward the targets on the in vitro tissue simulator. The robot then successfully punctured through the tissue simulator and injected pink dye. Lastly, the optical fiber steering task was showcased by steering an optical fiber and delivering focused light toward the targets by precisely adjusting the distance between the optical fiber and the chosen location. These demonstrations illustrate the potential of our SHY robots in different environments and applications, such as in food handling, manufacturing, and surgery.

As outlined in Supplementary Table 3, our proposed method provides several advantages compared to other methods. First, our method allows for the seamless integration of sensors into SHY robots with diverse degrees of freedom. While many methods detailed in the table encounter difficulties in sensor integration, those that attempt it often face constraints such as limited degrees of freedom or the requirement for a larger footprint to accommodate sensors. In contrast, sensors can be monolithically embedded into various designs and sizes of SHY robots. Furthermore, these modules can be assembled into multiple configurations, providing different degrees of freedom depending on the specific need. Second, our approach facilitates batch fabrication, as demonstrated in Supplementary Fig. 12. The ability to consistently build multiple modules simultaneously is a significant advantage in soft robotic applications. Other fabrication approaches present challenges in consistent reproducibility due to susceptibility to ambient conditions (i.e., temperature and humidity) and short operating windows[35]. In contrast, our proposed fabrication method possesses the benefit of being independent of environmental conditions and a long operating window, resulting in more reliable and consistent fabrication outcomes. Regarding mechanical performance, the SHY robotic modules exhibit comparable or better mechanical performance to other fluidically actuated soft robots fabricated in a layer-by-layer fashion. In terms of actuation speed, other soft robots fabricated through lamination-based methods achieve linear actuation speeds ranging from 0.42 to 223 mm/s and bending actuation speeds ranging from 0.145 to 2.09 rad/s[6,35,63]. While the actuation speeds achieved by these robots are generally comparable, some robots may achieve faster actuation speeds because they are pneumatically actuated (see Supplementary Table 3). Regarding output force, the SHY robotic modules exhibit comparable or higher output force considering the size of the robot (0.04 N/mm^2) in comparison to other soft robots (0.01 ~ 0.05 N/mm^2[26,53,55,58,63]). This demonstrates the strength of SHY robots in delivering force in the desired direction, leveraging the use of a mechanical controller.

Although the proposed SHY robotic technology has shown promising performance, there are remaining limitations that need to be addressed in future studies. First, SHY robotic modules require individual tubing to actuate each single DOF. The number of actuation lines can be reduced in the future with quake valves and fluid logic[67]. Next, as demonstrated in Fig. 6b, the relative error generally increases as the robot expands toward the end of its workspace. This increase in the relative error is due to the nonlinear behavior of the ionic resistive sensor, as demonstrated in Fig. 5c–e. To further improve the sensitivity of the sensor, the volume of the injected fluid could be optimized by tuning the size and shape of the PTFE soft-foldable actuator because the change in resistance across electrodes depends on the change in volume of the injected ionic solution. This fine-tuning of the actuator's dimensions could allow for a more linear relationship between the expansion state and sensor response. In addition, in this study, open-loop control was used to perform the pick-and-place, needle steering and tissue puncturing, and optical fiber steering tasks. Since the ionic resistive sensors embedded in the SHY robots exhibit a nonlinear, monotonic response, the sensing modality could be utilized for sensor feedback in robot position control in the future. By incorporating a real-time sensor feedback controller, the robot can respond and adapt to its environment, enabling more sophisticated and autonomous operation. Finally, the biocompatibility of films could be further explored. While the materials used in this work (i.e., fiber-reinforced epoxy laminate, polyimide, acrylic adhesive, and PTFE) are biocompatible, the presence of tinned copper films may introduce concerns[68,69]. To address this issue, additional exploration of biocompatible coatings and conductive materials can be done. Encapsulating the SHY robotic modules with a thin layer of Parylene C can be a viable solution to provide a biocompatible coating[68]. In addition, replacing the tinned copper films with gold could further enhance biocompatibility. These considerations would open up even more possibilities for a wide range of applications where the SHY robots can autonomously perform tasks with improved precision and adaptability for various applications.

Methods

Fabrication process

SHY robotic modules are fabricated using a layer-by-layer lamination technique. Various film materials are prepared by laser machining and chemical surface modification (via H_2 plasma) and bonded by heat pressing (Fig. 2, Supplementary Fig. 3, and Supplementary Movie 2). In this work, 254 µm thick fiber-reinforced epoxy laminate (McMaster Carr Supply Company) films are used as structural layers for the robots. Conductive traces and electrodes are created respectively with 50 µm thick copper film (McMaster Carr Supply Company). Polyimide films (CS Hyde Company) of 50 µm thickness are utilized as flexible joints. Acrylic sheet adhesive films (FR1500, DuPont de Nemours, Inc) are used to bond each film.

The fabrication process begins with laser precision micromachining (Fig. 2a) of various films using a diode-pumped solid-state (DPSS) ultraviolet (UV) laser (Coherent Matrix 355 nm, 5 W, laser precision micromachining system). After laser processing films, additional film preparation steps were taken on adhesive, copper, and 25 µm PTFE films (McMaster Carr Supply Company) before fully bonding all the films together. The shape-engraved adhesive films are selectively peeled off from the paper backing to bond to specifically selected locations (Fig. 2b). The copper films were coated with a layer of tin by submerging the sheet in a liquid tin (421A, MG Chemicals) for 3.5 min to prevent corrosion of the films (Fig. 2c). The PTFE films were exposed to H_2 gas plasma for 5 min at 450 W with a reactive ion etcher (790 Series, Plasma-Therm, LLC), where the chamber pressure was maintained at 100 mTorr and H_2 gas was constantly injected at a flow rate of 50 sccm into the chamber (Fig. 2d). Then, the structural layers with integrated sensors are prepared by bonding the tinned copper films and structural films.

To embed the ionic resistive sensor within the robot, adhesive films are transferred to the tinned copper films by aligning them using alignment pins and heat pressing them for 2 min at 100 °C with 350 kPa (Fig. 2e). The structural layers and the tinned copper films are then realigned and laminated for 5 min at 100 °C with 350 kPa to temporarily cure the layers together (Fig. 2f). Finally, excess tinned copper films are removed by laser cutting the sacrificial supports on the tinned copper films (Fig. 2g).

After preparing the necessary films, all the adhesive films are precured onto rigid or flexible films for 2 min at 100 °C with 350 kPa (Fig. 2h). All the films are then aligned using dowel pins, stacked in order, and laminated for 1.5 h at 200 °C with 350 kPa (Fig. 2i) to fully cure the adhesive and permanently bond them together. The hybrid robot modules are then released from the scaffold by laser cutting the sacrificial supports between the actuator and the scaffold (Fig. 2j). A microtubing (MRE025, Braintree Scientific, Inc.) with 304 µm inner diameter is attached to the robot using UV adhesive (NOA73, Norland Optical Adhesive) with a UV lamp (Sunspot 2, Uvitron International, Inc.) to provide a fluidic inlet channel (Fig. 2k). Two segments of 36 gauge wires are attached to the robot by soldering directly onto the electrodes.

Range of motion characterization

The range of motion of the SHY robotic modules was tested by fixing one end and allowing the other end to move freely with an electromagnetic (EM) position tracker (Aurora, Northern Digital Inc.). A syringe pump (Pump 11 Pico Plus Elite, Harvard Apparatus) was used to infuse and retract fluid into the SHY modules at a constant rate of 0.1 ml/min. The pressure of the actuation fluid was monitored using a pressure sensor (SSCDANT150PGAA5, Honeywell International, Inc.).

Output force characterization

The output force of the SHY robotic modules was characterized by measuring force versus pressure curves. The experiment involved testing the output forces at different expansion states, 0%, 25%, 50%, and 75% expansion. A syringe pump (Pump 11 Pico Plus Elite, Harvard Apparatus) was used to pressurize the actuation fluid at a constant rate of 0.1 ml/min, and pressurized up to 180 kPa. To measure the exerted force, a force/torque (F/T) sensor (NANO17, ATI Industrial Automation Inc.) was attached to a robotic arm (UR5e, Universal Robots) to position the F/T sensor perpendicular to the top surface of the modules.

Sensor characterization

The output voltage across the fixed resistance resistor (680 kΩ for 11.5 mm SHY robotic modules and 470 kΩ for 5 mm modules) of the voltage divider circuit (Supplementary Fig. 9) was measured to characterize the sensor in the SHY robotic modules. In this test, the syringe pump was used to infuse and retract actuation fluid at a constant rate of 0.1 ml/min, and the EM position tracker monitored the corresponding configuration of the SHY robotic module. During this test, 1 V peak to peak, 10 kHz sine wave was supplied to the voltage divider circuit, and the voltage across the fixed resistance resistor of the voltage divider circuit was constantly monitored using RMS to DC sensor (LTC1968, Analog Devices, Inc.) and ADC (NI USB-6210, National Instruments Corporation).

Data availability

The SHY continuum robot shape sensing data generated in this study are available at the public repository https://github.com/HunchanL/SHY-Robot.git. (https://doi.org/10.5281/zenodo.10937458) All the data supporting this study are provided in the main text and the Supplementary Information.

Code availability

The code to generate the shape-sensing plot in this study, along with sample data, is available at the public repository: https://github.com/HunchanL/SHY-Robot.git. (https://doi.org/10.5281/zenodo.10937458)

References

1. Perez, N. G. B. & Coad, M. M. Self-propelled soft everting toroidal robot for navigation and climbing in confined spaces. In *2022 IEEE/RSJ International Conference on Intelligent Robots and Systems (IROS)*, 5409–5415 (2022).
2. Zou, J., Lin, Y., Ji, C. & Yang, H. A reconfigurable omnidirectional soft robot based on caterpillar locomotion. *Soft Robot.* **5**, 164–174 (2018).
3. Ze, Q. et al. Spinning-enabled wireless amphibious origami millirobot. *Nat. Commun.* **13**, 3118 (2022).
4. Lee, Y.-W. et al. A tissue adhesion-controllable and biocompatible small-scale hydrogel adhesive robot. *Adv. Mater.* **34**, 2109325 (2022).

5. Hawkes, E. W., Blumenschein, L. H., Greer, J. D. & Okamura, A. M. A soft robot that navigates its environment through growth. *Sci. Robot.* **2**, eaan3028 (2017).
6. Van Lewen, D.et al. A millimeter-scale soft robot for tissue biopsy procedures. *Adv. Intell. Syst.* **5**, 2200326 (2023).
7. McCandless, M. et al. A soft robot for peripheral lung cancer diagnosis and therapy. *Soft Robot.* **9**, 754–766 (2022).
8. Kim, Y. et al. Telerobotic neurovascular interventions with magnetic manipulation. *Sci. Robot.* **7**, eabg9907 (2022).
9. Pittiglio, G. et al. Patient-specific magnetic catheters for atraumatic autonomous endoscopy. *Soft Robot.* **9**, 1120–1133 (2022).
10. El-Atab, N. et al. Soft actuators for soft robotic applications: a review. *Adv. Intell. Syst.* **2**, 2000128 (2020).
11. Wang, J. & Chortos, A. Control strategies for soft robot systems. *Adv. Intell. Syst.* **4**, 2100165 (2022).
12. Yang, G.-Z. et al. The grand challenges of science robotics. *Sci. Robot.* **3**, eaar7650 (2018).
13. Laschi, C., Mazzolai, B. & Cianchetti, M. Soft robotics: Technologies and systems pushing the boundaries of robot abilities. *Sci. Robot.* **1**, eaah3690 (2016).
14. Zhang, S. et al. Fabrication and functionality integration technologies for small-scale soft robots. *Adv. Mater.* **34**, 2200671 (2022).
15. Rich, S. I., Wood, R. J. & Majidi, C. Untethered soft robotics. *Nat. Electron.* **1**, 102–112 (2018).
16. Renda, F., Cianchetti, M., Giorelli, M., Arienti, A. & Laschi, C. A 3D steady-state model of a tendon-driven continuum soft manipulator inspired by the octopus arm. *Bioinspir. Biomim.* **7**, 025006 (2012).
17. Shiva, A. et al. Tendon-based stiffening for a pneumatically actuated soft manipulator. *IEEE Robot. Autom. Lett.* **1**, 632–637 (2016).
18. Becker, K. et al. Active entanglement enables stochastic, topological grasping. *Proc. Natl. Acad. Sci. USA* **119**, e2209819119 (2022).
19. Zhai, Y. et al. Desktop fabrication of monolithic soft robotic devices with embedded fluidic control circuits. *Sci. Robot.* **8**, eadg3792 (2023).
20. Rothemund, P., Kellaris, N., Mitchell, S. K., Acome, E. & Keplinger, C. Hasel artificial muscles for a new generation of lifelike robots-recent progress and future opportunities. *Adv. Mater.* **33**, 2003375 (2021).
21. Bluett, S., Helps, T., Taghavi, M. & Rossiter, J. Self-sensing electro-ribbon actuators. *IEEE Robot. Autom. Lett.* **5**, 3931–3936 (2020).
22. Davidson, Z. S. et al. Monolithic shape-programmable dielectric liquid crystal elastomer actuators. *Sci. Adv.* **5**, eaay0855 (2019).
23. Leroy, E. & Shea, H. Hydraulically amplified electrostatic taxels (haxels) for full body haptics. *Adv. Mater. Technol.* **8**, 2300242 (2023).
24. Ze, Q. et al. Soft robotic origami crawler. *Sci. Adv.* **8**, eabm7834 (2022).
25. Zhao, L. et al. Soft lattice modules that behave independently and collectively. *IEEE Robot. Autom. Lett.* **7**, 5942–5949 (2022).
26. Li, S. et al. Digital light processing of liquid crystal elastomers for self-sensing artificial muscles. *Sci. Adv.* **7**, eabg3677 (2021).
27. Xavier, M. S. et al. Soft pneumatic actuators: A review of design, fabrication, modeling, sensing, control and applications. *IEEE Access* **10**, 59442–59485 (2022).
28. Rus, D. & Tolley, M. T. Design, fabrication and control of soft robots. *Nature* **521**, 467–475 (2015).
29. Bai, H. et al. Stretchable distributed fiber-optic sensors. *Science* **370**, 848–852 (2020).
30. Baines, R. et al. Multi-modal deformation and temperature sensing for context-sensitive machines. *Nat. Commun.* **14**, 7499 (2023).
31. King, J. P., Valle, L. E., Pol, N. & Park, Y.-L. Design, modeling, and control of pneumatic artificial muscles with integrated soft sensing. In *2017 IEEE International Conference on Robotics and Automation (ICRA)*, 4985–4990 (IEEE, 2017).
32. Zhou, J. et al. A proprioceptive bellows (PB) actuator with position feedback and force estimation. *IEEE Robot. Autom. Lett.* **5**, 1867–1874 (2020).
33. Helps, T. & Rossiter, J. Proprioceptive flexible fluidic actuators using conductive working fluids. *Soft Robot.* **5**, 175–189 (2018).
34. Gupte, A., Kinnicutt, L., McDonald, K. & Ranzani, T. A soft ionic sensor for simultaneous pressure and strain measurements. In *2020 3rd IEEE International Conference on Soft Robotics (RoboSoft)*, 266–271 (IEEE, 2020).
35. Russo, S., Ranzani, T., Walsh, C. J. & Wood, R. J. An additive millimeter-scale fabrication method for soft biocompatible actuators and sensors. *Adv. Mater. Technol.* **2**, 1700135 (2017).
36. Sahu, S. K., Tamadon, I., Rosa, B., Renaud, P. & Menciassi, A. A spring-based inductive sensor for soft and flexible robots. *IEEE Sens. J.* **22**, 19931–19940 (2022).
37. Felt, W. et al. An inductance-based sensing system for bellows-driven continuum joints in soft robots. *Auton. Robots* **43**, 435–448 (2019).
38. Polygerinos, P. et al. Soft robotics: Review of fluid-driven intrinsically soft devices; manufacturing, sensing, control, and applications in human-robot interaction. *Adv. Eng. Mater.* **19**, 1700016 (2017).
39. Rus, D. & Sung, C. Spotlight on origami robots. *Sci. Robot.* **3**, eaat0938 (2018).
40. Chi, Y., Zhao, Y., Hong, Y., Li, Y. & Yin, J. A perspective on miniature soft robotics: Actuation, fabrication, control, and applications. *Adv. Intell. Syst.* **6**, 2300063 (2023).
41. Bilodeau, R. A., White, E. L. & Kramer, R. K. Monolithic fabrication of sensors and actuators in a soft robotic gripper. In *2015 IEEE/RSJ International Conference on Intelligent Robots and Systems (IROS)*, 2324–2329 (IEEE, 2015).
42. Grasso, G., Rosset, S. & Shea, H. Fully 3D-printed, stretchable, and conformable haptic interfaces. *Adv. Funct. Mater.* **33**, 2213821 (2023).
43. Della Santina, C., Duriez, C. & Rus, D. Model-based control of soft robots: A survey of the state of the art and open challenges. *IEEE Control Syst. Mag.* **43**, 30–65 (2023).
44. Della Santina, C., Bicchi, A. & Rus, D. On an improved state parametrization for soft robots with piecewise constant curvature and its use in model based control. *IEEE Robot. Autom. Lett.* **5**, 1001–1008 (2020).
45. Naughton, N. et al. Elastica: A compliant mechanics environment for soft robotic control. *IEEE Robot. Autom. Lett.* **6**, 3389–3396 (2021).
46. Gravagne, I. A., Rahn, C. D. & Walker, I. D. Large deflection dynamics and control for planar continuum robots. *IEEE/ASME Trans. Mech.* **8**, 299–307 (2003).
47. Ferrentino, P. et al. Finite element analysis-based soft robotic modeling: Simulating a soft actuator in sofa. *IEEE Robot. Autom. Mag.* 2–12 https://doi.org/10.1109/MRA.2022.3220536 (2023).
48. Chin, K., Hellebrekers, T. & Majidi, C. Machine learning for soft robotic sensing and control. *Adv. Intell. Syst.* **2**, 1900171 (2020).
49. Bruder, D., Fu, X., Gillespie, R. B., Remy, C. D. & Vasudevan, R. Koopman-based control of a soft continuum manipulator under variable loading conditions. *IEEE Robot. Autom. Lett.* **6**, 6852–6859 (2021).
50. Li, M., Pal, A., Aghakhani, A., Pena-Francesch, A. & Sitti, M. Soft actuators for real-world applications. *Nat. Rev. Mater.* **7**, 235–249 (2022).
51. Mengüç, Y., Correll, N., Kramer, R. & Paik, J. Will robots be bodies with brains or brains with bodies? *Sci. Robot.* **2**, eaar4527 (2017).
52. Abidi, H. & Cianchetti, M. On intrinsic safety of soft robots. *Front. Robot. AI* **4**, 5 (2017).
53. Niiyama, R. et al. Pouch motors: Printable soft actuators integrated with computational design. *Soft Robot.* **2**, 59–70 (2015).

54. Robertson, M. A., Kara, O. C. & Paik, J. Soft pneumatic actuator-driven origami-inspired modular robotic “pneumagami”. *Int. J. Robot. Res.* **40**, 72–85 (2021).
55. Li, S., Vogt, D. M., Rus, D. & Wood, R. J. Fluid-driven origami-inspired artificial muscles. *Proc. Natl. Acad. Sci.* **114**, 13132–13137 (2017).
56. Rus, D. & Tolley, M. T. Design, fabrication and control of origami robots. *Nat. Rev. Mater.* **3**, 101–112 (2018).
57. Ranzani, T., Russo, S., Schwab, F., Walsh, C. J. & Wood, R. J. Deployable stabilization mechanisms for endoscopic procedures. In *2017 IEEE International Conference on Robotics and Automation (ICRA)*, 1125–1131 (IEEE, 2017).
58. Yang, H. D., Greczek, B. T. & Asbeck, A. T. Modeling and analysis of a high-displacement pneumatic artificial muscle with integrated sensing. *Front. Robot. AI* **5**, 136 (2019).
59. Whitney, J. P., Sreetharan, P. S., Ma, K. Y. & Wood, R. J. Pop-up book MEMS. *J. Micromech. Microeng.* **21**, 115021 (2011).
60. Sreetharan, P. S., Whitney, J. P., Strauss, M. D. & Wood, R. J. Monolithic fabrication of millimeter-scale machines. *J. Micromech. Microeng.* **22**, 055027 (2012).
61. Lawton, R. A., Price, C. R., Runge, A. F., Doherty III, W. J. & Saavedra, S. S. Air plasma treatment of submicron thick PDMS polymer films: effect of oxidation time and storage conditions. *Coll. Surf. A Physicochem. Eng. Asp.* **253**, 213–215 (2005).
62. Borók, A., Laboda, K. & Bonyár, A. PDMS bonding technologies for microfluidic applications: A review. *Biosensors* **11**, 292 (2021).
63. Rogatinsky, J. et al. A collapsible soft actuator facilitates performance in constrained environments. *Adv. Intell. Syst.* **4**, 2200085 (2022).
64. Senftle, F., Grant, J. & Senftle, F. Low-voltage DC/AC electrolysis of water using porous graphite electrodes. *Electrochim. Acta* **55**, 5148–5153 (2010).
65. Lee, H. C., Pacheco, N. E., Fichera, L. & Russo, S. When the end effector is a laser: A review of robotics in laser surgery. *Adv. Intell. Syst.* **4**, 2200130 (2022).
66. Kang, E. T. & Zhang, Y. Surface modification of fluoropolymers via molecular design. *Adv. Mater.* **12**, 1481–1494 (2000).
67. McDonald, K. & Ranzani, T. Hardware methods for onboard control of fluidically actuated soft robots. *Front. Robot. AI* **8**, 720702 (2021).
68. Gafford, J. et al. Toward medical devices with integrated mechanisms, sensors, and actuators via printed-circuit mems. *J. Med. Devices* **11**, 011007 (2017).
69. Roina, Y., Auber, F., Hocquet, D. & Herlem, G. ePTFE functionalization for medical applications. *Mater. Today Chem.* **20**, 100412 (2021).

Acknowledgements

This work was supported by the National Center for Advancing Translational Sciences, National Institutes of Health, through Boston University Clinical & Translational Science Institute Grant Number 1UL1TR001430. Its contents are solely the responsibility of the authors and do not necessarily represent the official views of the National Institutes of Health. This work was also partially supported by the National Science Foundation Research Experiences for Undergraduate Sites in Integrated Manufacturing, EEC-1852255. The authors would like to acknowledge Boston University BioInterface Technologies Facility for providing access to the contact angle goniometer used in this research.

Author contributions

S.R. designed and supervised the study. H.L. and S.R. designed robots and necessary experiments. H.L., N.E., M.L., S.S., E.V., S.J., and H.C. fabricated robots, performed the experiments, and analyzed experimental and analytical model data. H.L., N.E., and S.R. drew figures and wrote the manuscript. All authors reviewed the manuscript.

Competing interests

The authors declare the existence of a financial/non-financial competing interest.

Additional information

Supplementary information The online version contains supplementary material available at https://doi.org/10.1038/s41467-024-51137-8.

Correspondence and requests for materials should be addressed to Sheila Russo.

Peer review information *Nature Communications* thanks Hemma Philamore and the other anonymous, reviewer(s) for their contribution to the peer review of this work. A peer review file is available.